RSC Advances

PAPER

View Article Online
View Journal | View Issue



Cite this: *RSC Adv.*, 2024, **14**, 32251

# Al, P-co-doping and interface engineering synergistically boost the electrocatalytic performance of $WS_2/Ni_3S_2/NiS$ nanosheet heterostructure for efficient hydrogen evolution reaction†

Mghaib Al Shahrani, Mabrook S. Amer, * Ahmad A. Alsaleh, Prabhakarn Arunachalam and Abdullah M. Al-Mayouf *

The fabrication of earth-abundant electrocatalysts capable of facilitating hydrogen evolution reactions (HER) is essential for creating sustainable hydrogen fuel by water splitting. Here, we present a one-pot hydrothermal approach for producing aluminum and phosphorus co-doped $NiS/Ni_3S_2/WS_2$ heterostructure hybrid frameworks on nickel foam. The optimal Al and Al, P/NiWS-b@NF catalyst exhibits high HER activity with overpotentials of 139 and 227 mV at current densities of 10 and 50 mA $cm^{-2}$, respectively, thanks to the synergistic effect of the various constituents of the catalyst. What is more, it also exhibits a promising Tafel slope of 124 mV $dec^{-1}$ and is electrocatalytically durable for 10 hours in 0.5 M $H_2SO_4$ solution. The high HER activity of Al, P/NiWS-b@NF could be explained by the large number of active sites of the hierarchical heterostructure and electron effects produced by the combination of interfacial and aluminum and phosphorus doping.

Received 13th August 2024
Accepted 30th September 2024

DOI: 10.1039/d4ra05868b

rsc.li/rsc-advances



## 1. Introduction

Energy consumption growth poses a significant challenge regarding sustainability and environmental impact.[1–3] Hydrogen has the potential to play a significant role as an energy carrier and the transition to a more sustainable energy future, as it is clean, efficient, renewable, and highly energy dense, making it an ideal energy storage and transportation option.[4] The electrolysis of water is certainly considered one of the most sustainable techniques for producing hydrogen. The process involves splitting water molecules ($H_2O$) into hydrogen and oxygen using electricity obtained from renewable energy sources such as solar and wind power, which has a thermodynamic potential of 1.23 V.[4–7] However, water electrolysis for hydrogen production poses significant challenges due to the inherent dynamic overpotentials in HER and the oxygen evolution reaction (OER).[8] Consequently, the design and optimization of electrocatalysts for HER and OER can contribute to achieving a reduction in overpotentials as well as enhanced reaction kinetics. Platinum-based materials are usually recognized as excellent catalysts for HER due to their outstanding catalytic activity and durability.[9] Still, due to the high cost and limited availability of platinum, widespread commercial adoption of water electrolysis for hydrogen production remains a challenge.[10,11] Recent research efforts are ongoing to explore a wide range of HER earth-abundant transition metal electrocatalysts, including metal alloys, metal oxides, nitrides, sulfides, selenides, and carbon-based materials.[9,12–17] Among these catalysts, transition metal sulfide (TMS)-based electrocatalysts have emerged as promising materials for various electrochemical reactions, including water electrolysis for hydrogen production.[18] However, the limitations associated with pure TMSs such as their unfavorable free energy of hydrogen adsorption ($\Delta G_{H^*}$) values, inability to facilitate water dissociation, and their high resistance coupled with conductivity due to a large band gap, pose significant challenges for their use as effective electrocatalysts, particularly in the HER during water electrolysis. Due to these limitations, designing and fabricating high-efficiency and highly stable TMS catalysts for the HER is both an interesting challenge and an exciting opportunity.

Catalysts have high activity due to their synergistic effects, which include electron transmission speed, reaction energy barrier, electroactive sites where reactions occur, and electroactive sites' capacity.[19] As an example, surface and interface engineering can be applied to enhance the electrocatalyst performance. A number of methods, for example, can be used to prepare some vacancies, dislocations, and grain boundary

*Electrochemical Sciences Research Chair (ESRC), Chemistry Department, College of Science, King Saud University, P. O. Box 2455, Riyadh 11451, Saudi Arabia. E-mail: msamer@ksu.edu.sa; amayouf@ksu.edu.sa*

† Electronic supplementary information (ESI) available. See DOI: https://doi.org/10.1039/d4ra05868b

defects by using (1) plasma treatment,[20] (2) common doping methods can improve the catalyst's composition and electrical properties,[21] and (3) heterogeneous structures can be designed to provide high energy interfaces for catalytic reactions.[22] Interfacial effects play a big role in engineering electrocatalysts to be catalytically active, selective, and stable by regulating how adsorbents, intermediates, and electrons are bound, transformed, and transferred at the boundary of two domains.[20,22–25] By modifying the interfacial characteristics of TMSs, low-dimensional materials could be prevented from aggregating, while charge and mass transfer can be accomplished efficiently.[26,27] Further, interface engineering might enrich the active sites and promote electron redistribution, therefore regulating both the adsorption and desorption of intermediates and improving the efficiency of HER.[28] Among the TMS electrocatalysts, tungsten disulfide ($WS_2$) is widely used as an HER catalyst because of its high electrochemical efficiency.[29–31] The development of heterostructures has been a key way to overcome $WS_2$ electrocatalysts limitations by attaining electronic transformations, thereby improving efficiency and expanding active surface areas.[32] Researchers have studied various $WS_2$-based heterostructures for improving the role of $WS_2$ as HER electrocatalysts, such as $MoS_2$, $CoSe_2$, and $WSe_2$. Various $WS_2$-based heterostructures, including $MoS_2$, $CoSe_2$, and $WSe_2$, have been considered to enhance the characteristics of $WS_2$ as an electrocatalyst for HER.[33–35] Co-doping of metals over tungsten sulfide heterojunction catalysts for HER has only been reported in rare cases. It is therefore necessary to advance a facile approach for preparing tungsten sulfide heterojunctions to further improve HER activity.

Herein, we propose a facial one-pot fabrication of Al, and P element co-doped into a hierarchical NiWS@NF heterostructure hybrid framework consisting of Ni-sulfides (NiS, and $Ni_3S_2$) nanoparticles and $WS_2$ nanosheets supported on Ni-foam (NF) to promote HER kinetics on metal sulfides. Given the available hierarchical structures constructed for this study, it was found that the optimal Al, P/NiWS-b@NF catalyst had the superior catalytic features for the HER, exhibiting lower overpotentials of 139 and 227 mV at current densities of 10 and 50 mA $cm^{-2}$, correspondingly. Moreover, it displays a favorable Tafel slope of 124 mV $dec^{-1}$ in 0.5 M $H_2SO_4$ solution for the HER. Based on the obtained results, multi-interface collaboration, Al, and P doping are associated with superior performance in hierarchical NiWS@NF hybrid frameworks.

# 2. Experimental

## 2.1 Chemicals and materials

The regents were all analytical grade without additional purification. Sodium hypophosphite monohydrate ($NaH_2PO_2 \cdot H_2O \geq$ 99.0%), aluminum nitrate hexahydrate ($Al(NO_3)_3 \cdot 6H_2O \geq$ 98.0%), and sodium tungstate dihydrate ($Na_2WO_4 \cdot 2H_2O \geq$ 99.0%) were acquired from Alfa Aesar and used as the P, Al, and W precursors, respectively. Thiourea ($(NH_2)_2CS \geq$ 99.0%), and hydroxylamine hydrochloride ($NH_2OH \cdot HCl \geq$ 98.0%) were purchased from Sigma-Aldrich and utilized as sulfur sources and reducing agents, respectively. Potassium hydroxide belts (KOH $\geq$ 85.0%), nitric acid ($HNO_3$ 68–70%), isopropanol ($C_3H_8O \geq$ 99.0%), and Nafion ($C_9HF_{17}O_5S$ 5%) were obtained from Sigma-Aldrich. Nickel foam (1.7 × 200 × 300 mm, NF $\geq$ 99.0%) was purchased from Xiamen Zopin New Material Limited Company.

## 2.2 Synthesis of the hierarchical NiWS@NF, and Al, P/NiWS@NF hybrid framework

In general, commercial NF, which is available in an area of 2 × 5 $cm^2$, is typically used as both a nickel source and template. NF was cleaned with 3 M HCl solution, acetone, and anhydrous ethanol in sequence for 15 min each through sonication. It was lastly dried in air and kept for future use. The NiWS@NF and Al, P/NiSW-*x*@NF electrocatalysts were prepared using a hydrothermal-directed method. Typically, in 25 mL DI water, 1 mM $Na_2WO_4 \cdot 2H_2O$, 1 mM $NaH_2PO_2 \cdot H_2O$, 6 mM $NH_2CSNH_2$, and 2 mM $NH_2OH \cdot HCl$ are dissolved by gentle magnetic stirring, and a clear solution is obtained. Following that, 25 mL of DI water including 0.2 mM $Al(NO_3)_3 \cdot 6H_2O$ was submerged independently and introduced dropwise to the first mixture solution while stirring magnetically. After the transfer of the mixture to a 100 mL Teflon-lined autoclave, the NF was kept in the previous solution and heated at 180 °C for 14 hours. Upon the reaction being complete, Al, P/NiWS-*x*@NF was thoroughly rinsed using an ethanol and water mixture prior to getting vacuum-dehydrated using a furnace at 60 °C overnight.

## 2.3 Synthesis of control samples

To produce nickel sulfide, tungsten sulfide nanostructures on NF (NiWS@NF), aluminum-doped tungsten sulfide nanostructures on NF (Al/NiWS@NF), and P-doped $WS_2$ nanostructures on NF (P/NiWS@NF), the hydrothermal reaction was carried out similarly. To achieve this, the appropriate precursor salts were incorporated in the required molar ratios. After heating to 180 °C for 14 hours, they were dried overnight at 60 °C in a vacuum oven.

## 2.4 Preparation of a Pt/C reference electrode on NF

The synthesized electrodes were compared to commercial electrodes using a Pt/C catalyst loaded onto NF substrates. Typically, 950 μL of water and isopropyl alcohol (v/v = 1 : 1) were mixed with 5 mg of Pt on carbon (20 wt%) catalyst and 20 μL of Nafion (5 wt%). The solution was then stirred by sonication for 30 minutes. After spreading Pt/C ink to the raw NF surface in a 1 × 1 $cm^2$ geometric area, the electrode was dried in a vacuum oven at 60 °C.

## 2.5 Characterization

The high-resolution scanning electron microscope (HRSEM) photographs were observed on a Hitachi S4800 (Japan) that was functioned at 1.0 kV and 10 mA. To study the nanometric details of the samples and thin film deposited morphologies, a high-resolution transmission electron microscope JEOL 2100F microscope (Japan) at 200 kV is employed with an energy dispersive X-ray (EDX) detector. To conduct TEM analysis,

 

samples were suspended in ethanol solution and mounted on a Cu grid with a holey carbon film. The crystallinity, purity, and phases of materials were measured using a MiniFlex-600 (Rigaku) with a Cu Kα irradiation technique (40 kV voltage, 15 mA current). An X-ray photoelectron spectrometer (Escalab 253, Thermo Fisher Scientific) with a monochromated MgKα X-ray source has been employed for X-ray photoelectron spectroscopy (XPS) analysis of the produced catalyst. To calibrate the binding energy (BE) scale, the C 1s component of aliphatic hydrocarbons has been used, with a BE value of 285.0 eV.

### 2.6 Electrochemical measurements

A potentiostat (BioLogic SAS, model) was used to conduct electrochemical measurements on three electrodes, with NiWS@NF catalysts, Al, P/NiWS-*x*@NF catalysts working electrodes, and carbon graphite rods and saturated silver/silver chloride electrodes serving as counter and reference electrodes, respectively. HER activity of NiWS@NF and Al, P/NiWS-*x*@NF catalysts in 0.5 M $H_2SO_4$ was investigated using linear sweep voltammetry (LSV) at a scanning rate of 5 mV $s^{-1}$ with a potential window varying from 0.20 to −0.6 $V_{RHE}$. The LSV plots were analyzed without *IR* compensation. In electrochemical impedance spectroscopy (EIS) measurements, the same cell configuration was used at the chosen potential and at frequencies between 200 MHz and 100 Hz with amplitudes of 10 mV. All electrochemical analysis were carried out under normal atmospheric pressure and at 25 °C under nitrogen purge. Electrochemical surface area (ECSA) and double-layer capacitance ($C_{dl}$) were evaluated at various scanning speeds from 10 to 100 mV $s^{-1}$ in non-faradaic areas.

## 3. Results and discussion

### 3.1 Electrocatalysts preparation and characterization

Several tungsten sulfide/nickel sulfide-based electrocatalysts were synthesized and studied for HERs. Various proportions of aluminum and/or phosphorus were incorporated into nickel sulfide and tungsten sulfide hybrid structures, which were termed Al, P/NiWS-a@NF (the same amount of Al to P), Al, P/NiWS-b@NF (Al < P), and Al, P/NiWS-c@NF (Al > P) (Table S1†). The second series includes pure NiWS@NF, and single-element doped electrocatalysts *i.e.* (Al/NiWS-d@NF, and P/NiWP-e@NF). Fig. 1 shows how the Al, P/NiWS-*x*@NF heterostructure was produced *via* a facial hydrothermal reaction. For the synthesis of NiWS@NF nanosheets, Ni foam having a porous structure served as the growth support and Ni source. Since metallic Ni has high reactivity, it readily reacts with thiourea to form trigonal T-NiS/T-$Ni_3S_2$ nanoparticles on NF. As a result of the highly reactive $S^{2-}$ on the T-NiS/T-$Ni_3S_2$ surface and the numerous nucleation sites provided by the nanoparticles, high-density hexagonal H-$WS_2$ nanosheets were then formed on the T-NiS/T-$Ni_3S_2$ nanosheets using a hydrothermal method.[22]

To identify the crystal structure of the obtained catalysts, the XRD measurement of fabricated NiWS@NF, Al/NiWS@NF, P/NiWS@NF, and Al, P@NiWS-*x*@NF, materials were recorded, as depicted in Fig. 2a and S1a.† In Fig. 2b, except for the indexed $WS_2$ peaks of 2$\theta$ about 14.36, 32.77, 33.59, 35.94, 39.60, and 49.80° which correspond to the (002), (100), (101), (102), (103), (221), and (105) planes for hexagonal H-$WS_2$ (card no. 01-084-1398), all of the characteristic peaks at the 2$\theta$ of 21.93, 31.13, 38.41, 38.69, 44.73, 50.24, 50.47, and 55.50° are extremely compatible with 101, 110, 021, 003, 202, 211, 113, and 122 planes of trigonal T-$Ni_3S_2$ phase (card no. 01-085-0775). Furthermore, other obvious peaks were also observed at the 2$\theta$ of trigonal phase T-NiS planes (card no. 01-074-7240), demonstrating that the nanocomposites are composed of $WS_2$, $Ni_3S_2$, and NiS.[36] It is evident from the observed sharp diffraction peaks that NiWS@NF materials doped with Al or P have greater crystallinity. Fig. S1b† displays a diffraction peak location shift after Al and/or P insertion in the pure NiWS@NF sample, which can be attributed to lattice expansion. There were no additional diffraction peaks observed, signifying that the bimetallic

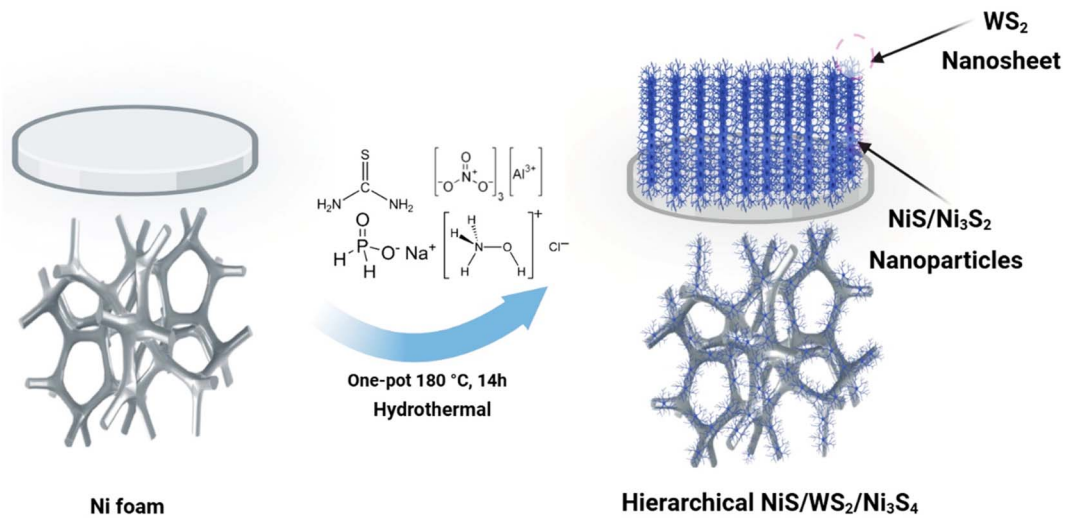


Fig. 1 Schematic representation for hetero-structured Al, P/NiWS-*x*@NF composite fabrication.

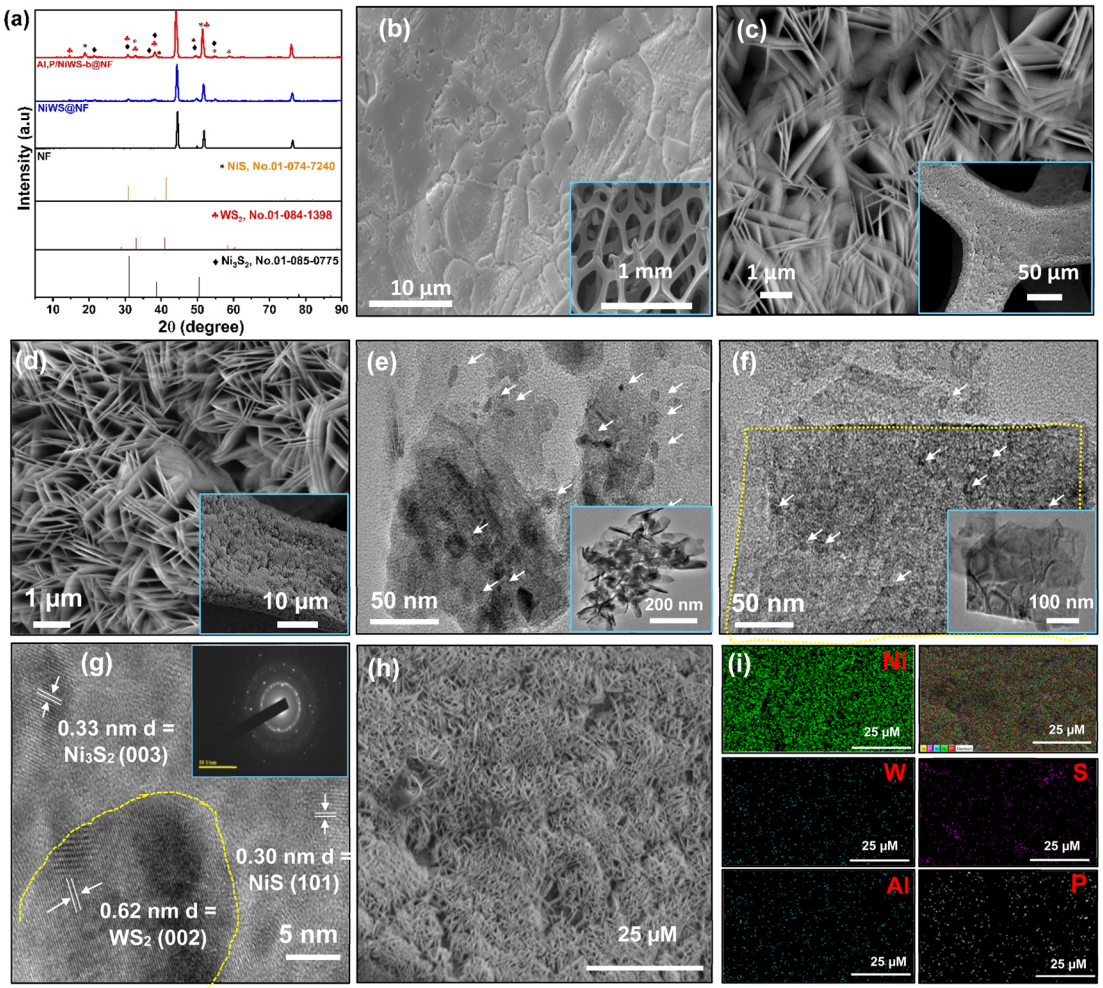


Fig. 2 (a) XRD patterns of the NF, NiWS@NF, and Al, P/NWS-b@NF. (b) SEM photographs of bare NF and (c) NiWS@NF, and Al, P/NWS-b@NF (d). (e and f) TEM images of the NiWS@NF, and Al, P/NWS-b@NF samples, respectively. (g) HR-TEM images of Al, P/NiWS-b@NF. Inset are the corresponding SAED patterns obtained on a single nanosheet. (h and i) Corresponding elemental mapping of Al, P/NWS-b@NF.

doping process does not change the crystalline phases. HR-SEM was used to evaluate the morphologies of various materials. As can be seen in Fig. 2b, the NF was composed of a porous Ni framework, and the inset of Fig. 2b shows the Ni skeleton's smooth surface. After the hydrothermal reaction, *in situ* grown NiWS@NF nanosheets having a mean diameter of 80 nm were formed (Fig. 2c and d). According to the HR-SEM images (inset of Fig. 2c and d), NiWS nanosheets had smooth surfaces. As shown in Fig. 2d, HR-SEM imaging reveals that the sample's surface appears to be comprised of nanoflakes–nanosheet assemblies. The top view of the framework in Fig. 2c and d confirms that the nanosheet assemblies are very uniform. Moreover, the top view of the Al, P/NiWSAlP-b@NF framework indicates that $WS_2$ nanosheets and NiS/$Ni_3S_2$ nanoparticles are strongly linked, suggesting that NiS/$WS_2$ and $WS_2$/$Ni_3S_4$ interfaces are abundant. As a result of the *in situ* growth of NiWS nanosheets, there was very high structural stability, which prevented most of the bubbles that were generated during electrocatalysis from damaging electrocatalysts, thus promoting the stability of the HER catalyst.[37] To further illustrate the locally assembled structure of the heterostructure frameworks, transmission electron microscopy was applied to both the NiWS@NF and Al, P/NiWS-d@NF heterostructures. Fig. 2e and f show the low-magnification TEM image of NiWS@NF, and Al, P/NiWS-b@NF heterostructure respectively. In Fig. 2e and f, the TEM image of NiWS@NF, and Al, P/NiWS-b@NF heterostructure, a large granular component, about a few tens of nanometers in size, is thought to be T-NiS/T-$Ni_3S_2$. It is easy to identify H-$WS_2$ nanosheets by their distinguishable lateral lamellar stripes, ranging in size from a few nanometers to tens of nanometers (Fig. 2f and S2†). Furthermore, HR-TEM images of Fig. 2g reveal a distinct interface between H-$WS_2$–T-NiS and T-NiS–T-$Ni_3S_2$, indicating heterojunction formation. As illustrated in Fig. 2g and S2d,† the electron diffraction patterns produced in the selected area of the sample confirm the presence of H-$WS_2$, T-NiS, and T-$Ni_3S_2$. With the help of HR-TEM (Fig. 2g and S2d†), we have studied the structure of NiWS@NF as well as Al, P/NiWS-b@NF heterostructures. The hexagonal phase of the H-$WS_2$ nanosheet's (002) crystalline plane has a lattice spacing of 0.62 nm.

A crystalline plane with a lattice spacing of 0.30 nm and 0.24 nm indicates the presence of planes (101) and (220) in the trigonal phase of T-NiS nanoparticles. The (220) plane, which has a lattice spacing of 0.33 nm, reveals the presence of the trigonal phase of the T-$Ni_3S_2$ crystal structure. To validate the elemental composition of the NiWS@NF, and Al, P/NiWS-b/NF samples, HR-SEM (Fig. S3a–f† and 2i) and energy dispersive X-ray (EDS, Fig. S4 and S5†) color mapping was performed. The elemental mapping analysis of NiWS@NF, and Al, P/NiWS-b@NF verified that the spatial distribution of W, Ni, S, and P elements was uniform, as shown in Fig. S3a–f† and 2i. Consequently, $WS_2$ nanosheets and NiS/$Ni_3S_2$ nanoparticles were crosslinked to produce an exceptionally accessible and abundant heterogeneous interface in the Al, P/NiWS-b@NF framework. According to EDS analysis of Al, P/NiWS-b@NF sample, Ni : S : W : Al and P had weight ratios of 60.33 : 26.34 : 11.22 :

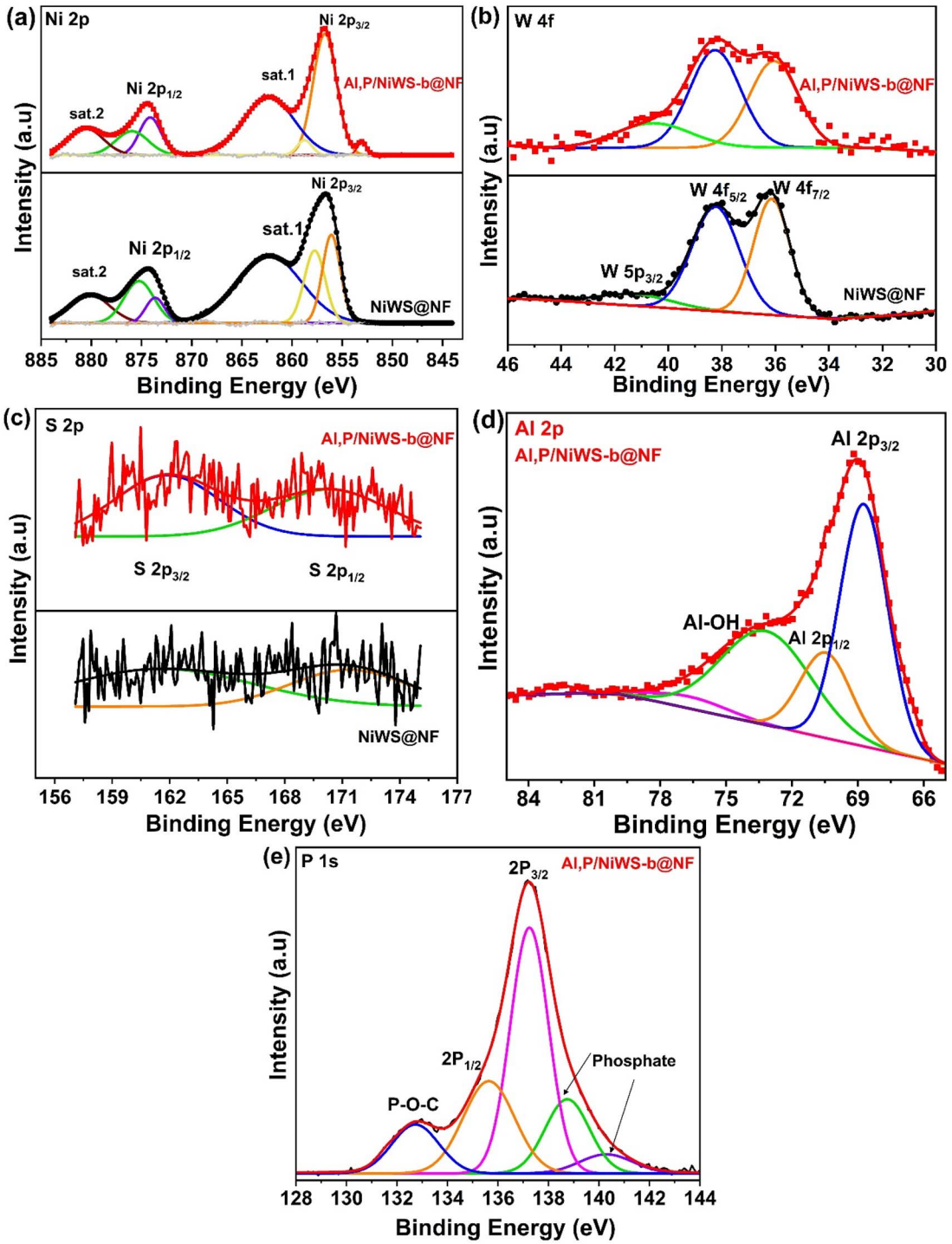


Fig. 3 Elemental XPS spectra of (a) Ni 2p, (b) W (4f), (c) S 2p, (d) Al (2p), and (e) P 2p of NiWS@NF, and Al, P/NiWS-b@NF.

0.81 : 1.29 (Fig. S4†). This HR-SEM image, as well as an accompanying elemental map, confirmed the homogeneous dispersion of Ni : S : W : Al and P in the Al, P/NiWS-b@NF heterostructure. To reveal the surface elements, chemical states and composition, XPS spectrum analysis was performed on NiWS@NF and Al, P/NiWS-b@NF heterostructure catalysts. Fig. S6† illustrates the full XPS spectrum for NiWS@NF, P/NiWS@NF, Al/NiWS@NF, and Al, P/NiWS-b@NF which reveals W, Ni, S, Al, and P in the sample. As seen in Fig. 3a, the Ni 2p spectrum of NiWS@NF, and Al, P/NiWS-b@NF shows binding energies at about 853.1 eV, 870.5 eV, and 854.3 eV, 874.6 eV, corresponding to the spin–orbit characteristics of $Ni^{2+}$ and $Ni^{3+}$, respectively.[37,38]

There is an obvious shift in Ni 2p peak positions between Al, P/NiWS-b@NF compared to the pristine NiWS@NF, as a result of charge transfer through heterostructure interfaces. Fig. 3b shows XPS peaks for W 4f. A four-component spectrum can be deconvoluted from the W 4f spectrum. The peaks at 36.20 eV and 38.22 eV agree to W $4f_{7/2}$ and W $4f_{5/2}$ in H-$WS_2$.[36,37] In addition, the peak at 41.05 eV is expected to originate from oxidation species such as W $5p_{3/2}$. There is a positive shift in W $4f_{7/2}$ from 36.20 eV for pure NiWS@NF to 36.0 eV for Al, P/NWS-b@NF (Fig. 3b). The spectra of S 2p are revealed in Fig. 3c. There are two peaks at binding energies of 161.92 and 170.88 eV that belong to the S $2p_{3/2}$ and S $2p_{1/2}$ components of S in NiWS@NF, and Al, P/NiWS-b@NF, respectively.[37,38] Fig. 3d displays the high-resolution peaks of XPS of Al 2p in Al, P/NiWS-b@NF. BE signals at 70.55 eV and 68.81 eV reveal the characteristic peaks of $Al^{3+}$ states, which are Al $2p_{3/2}$ and Al $2p_{1/2}$ respectively.[39,40] The spectrum of P 2p is shown in Fig. 3e. As shown in Fig. 3e, air-oxidized phosphorus could have produced two peaks with high binding energies (138.74 and 140.31 eV). Moreover, existing two peaks were situated at 135.63 eV and 137.19 eV, which may be read as the BEs of P $2p_{1/2}$ and P $2p_{3/2}$, accordingly, that corroborate the existence of an interaction across nonmetal/metal and P in Al, P/NiWS-b@NF.[34,35] The results demonstrate the composition of elements, proving the effective creation of nanosheets in Al, P/NiWS-b@NF heterojunction frameworks using a simple hydrothermal self-organized procedure. Furthermore, the chemical state changes in Ni, and W elucidate the development of highly coupled interfaces between H-$WS_2$, and T-NiS/T-$Ni_3S_2$ *via* powerful electronic interactions. In this way, metal sulfides can be manipulated to control the adsorption and desorption energies of reaction intermediates by manipulating their frontier orbital energies.[41–45]

### 3.2 Electrochemical HER performance

Al, P/NiWS-*x*@NF electrocatalysts displays the above advantages, such as a heterointerface and high mass and charge transfer capabilities, which indicates it may be a good electrocatalyst for HER. A conventional three-electrode–electrolyte medium containing $N_2$-saturated 0.5 M $H_2SO_4$ solution and graphite rod as the counter electrode was used to evaluate the catalytic features of all the as-made electrocatalysts. According to Fig. S8a and b† HER performance was compared at Al, P/NiWS-b@NF growth times of 6 h, 10 h, 14 h, and 18 h. It was evident that Al, P/NiWS-b@NF 14 h demonstrated the best HER activity. During the 14 hour growth process, H-$WS_2$ nanosheet density increased continuously, enabling more active edge sites. Based on Fig. 4a, the polarization curves clearly reveal that Al, P/NiWS-b@NF has the same activity as commercial Pt/C (20 wt%) at low potential, and even becomes preferable to commercial Pt/C when current density reaches 210 mA $cm^{-2}$ (inset in Fig. 4b, left). In addition, Al, P/NiWS-b@NF catalyst reveal improved HER performance at current densities of 10 and 50 mA $cm^{-2}$, which are much lower than those of Al, P/NiWS-a@NF, Al, P/NiWS-c@NF, NiNW@NF, Al/NiNW@NF, P/NiNW@NF and NF (Fig. 4a and b), due to the highly exposed and rich heterointerfaces in the T-NiS/H-$WS_2$/T-$Ni_3S_2$ framework, which encourages HER. As P and Al are introduced into NiWS@NF, hierarchical nanosheet heterostructures are formed and the elemental composition is modulated to enhance HER activity. Fig. 4c shows Al, P/NiWS-b@NF exhibiting an overpotential of 139, and 227 mV to afford 10, and 50 mA $cm^{-2}$ current density, much lesser than Al/NiWS@NF (182, and 268 mV), P/NiWS@NF (202, 308 mV), and NiWS@NF F (285, and 361 mV). A smaller overpotential at Al, P/NiWS-b/NF indicates fast HER kinetics and high catalytic activity, as illustrated in Fig. 4c.

Compared to NiWS@NF catalyst electrodes, Al, P/NiWS-b@NF exhibit superior HER activities, indicating that a heterostructure formed by NiS/$Ni_3S_2$ and Al, P/NiWS should be able to enhance $WS_2$ HER. Thus, the improved electrocatalytic features of the synthesized heterostructures can be attributed to the synergistic interactions between the different dopants and host materials. By introducing Al and P, electronic conductivity and active site availability are improved, resulting in higher HER activity. Additionally, the unique morphology and high surface area of the NiS/$Ni_3S_2$/$WS_2$ heterostructures further facilitate efficient hydrogen production. As part of the analysis of the HER kinetics, Tafel plots and a Tafel slope value were also utilized (Fig. 4d) to regulate the next step of the HER using the Tafel equation; $\eta = a + b\log j$.[46] In general, HER involves two stages, hydrogen adsorption and hydrogen desorption. Hydrogen adsorption occurs through the Volmer reaction, $H^+ + M + e^- \rightarrow M\text{–}H_{ads}$ (where stands for active site and H represents absorbed hydrogen) and desorption occurs through either Heyrovsky, $M\text{–}H_{ads} + H^+ + e^- \rightarrow M + H_2$ or Tafel reactions, $2M\text{–}H_{ads} \rightarrow 2M + H_2$ in an acidic medium. As reported, the Volmer, Heyrovsky, and Tafel reactions possess Tafel slopes of 120, 40, and 30 mV $dec^{-1}$, respectively.[47] Commercial 20% Pt/C had a Tafel slope of 54 mV $dec^{-1}$, which is similar to what has been reported.[48] It follows that Al/NiWS@NF and Al, P/NiWS-b/NF have the lowest Tafel slope values of 114 and 124, respectively, and follow the order NF (243 mV $dec^{-1}$) > P/NWS@NF, (152 mV $dec^{-1}$) > NiWS@NF, (128 mV $dec^{-1}$). According to Tafel slope values for Al, P/NiWS-b/NF in an acidic medium, HER is processed *via* the Heyrovsky mechanism.[49] In other words, the smaller Tafel values indicate more efficient kinetics and greater electrocatalytic features of Al, P/NiS/$WS_2$/$Ni_3S_4$ towards the HER. Furthermore, the electrochemical double-layer capacitances ($C_{dl}$) measured in non-faradaic conditions were examined to determine the ECSA for the developed electrode materials (Fig. S7† and 4e). In Fig. 4e, Al, P/NiWS-b@NF

 

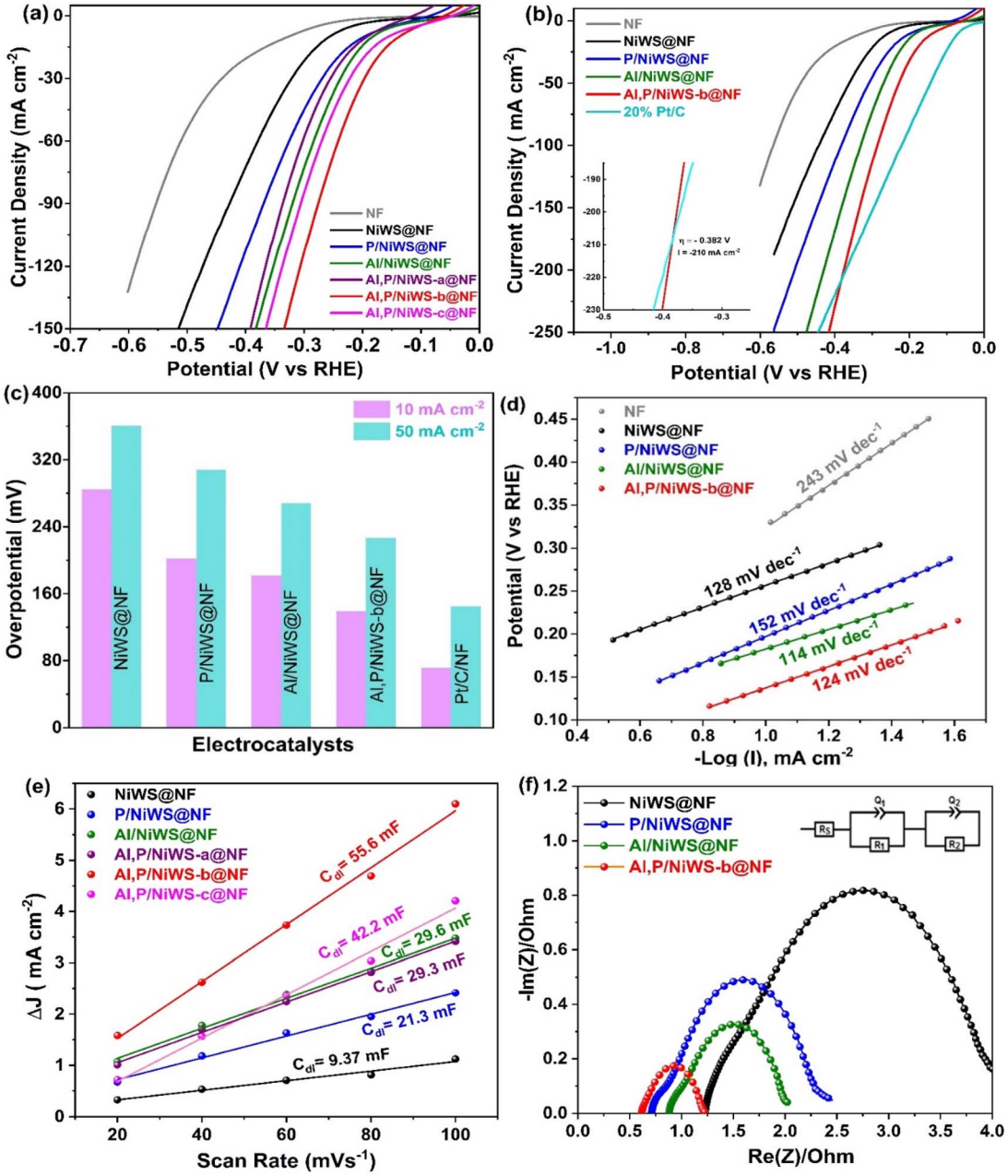


Fig. 4 Electrochemical HER features: (a and b) LSV HER polarization curves (c) overpotentials of various samples at the current densities of 10 mA $cm^{-2}$, and 50 mA $cm^{-2}$ for HER. (d) Tafel plots, (e) $C_{dl}$, and (f) Nyquist plots of various samples.

revealed a significantly higher $C_{dl}$ (55.6 mF $cm^{-2}$) than Al, P/NiWS-c@NF (42.2 mF $cm^{-2}$), Al, P/NiWS-a@NF (29.3 mF $cm^{-2}$), P/NiWS@NF (21.3 mF $cm^{-2}$), Al/NiWS@NF (29.6 mF $cm^{-2}$), and NiWS@NF (9.37 mF $cm^{-2}$). According to $C_{dl}$ values, Al, P/NiWS-b@NF exhibits a strong increase in ESCA, indicating that Al and P doping can increase ESCA and increase HER accessibility. It validates that the $Ni_3S_2/WS_2$ heterostructure has a higher exposure to efficient active sites, which contributes to its exceptional HER features as seen in Fig. 4a. Furthermore, the crosslinked H-$WS_2$ nanosheet (Fig. 2f, HR-TEM images) as well as the abundant T-NiS/T-$WS_2$ and H-$WS_2$/T-$Ni_3S_2$ heterojunction in Al, P/NiWS-b@NF are regarded as major contributors to the increase in the ECSA value of Al, P/NiWS-b@NF. Electrocatalyst capacitance and interfacial properties at active state are investigated by EIS measurements (Fig. 4f, and Table 1). The smallest charge transfer resistance ($R_{ct}$) was obtained for Al, P/NiWS-b@NF (0.683 ohm) compared to the reference's catalysts (Table 1) suggesting that electron transfer kinetics are much faster at the electrode–electrolyte interface. Considering the lowest $R_{ct}$ value for Al, P/NiWS-b@NF, it implies that there is a higher intrinsic conductivity present in the hybrid framework that is responsible for rapid electron transport kinetics in the electrocatalytic HER. By creating a heterointerface between $Ni_3S_2$ and $WS_2$, the electronic

Table 1 Hydrogen evolution reaction electrochemical properties of electrocatalysts

| Electrocatalyst | $\eta$ (mV *vs.* RHE) @ $J = -10$ mA cm$^{-2}$ | $\eta$ (mV *vs.* RHE) @ $J = -50$ mA cm$^{-2}$ | Tafel slope (mV dec$^{-1}$) | $C_{dl}$ (mF cm$^{-2}$) | $R_{ct}$ ($\Omega$ cm$^2$) |
|---|---|---|---|---|---|
| NF | 322 | 494 | 283 | — | — |
| NiWS@NF | 285 | 361 | 128 | 9 | 3.20 |
| P/NiWS@NF | 202 | 308 | 152 | 21 | 3.19 |
| Al/NiWS@NF | 3 | 182 | 114 | 30 | 2.43 |
| Al, P/NiWS-a@NF | 195 | 288 | — | 29 | — |
| Al, P/NiWS-b@NF | 139 | 227 | 124 | 56 | 0.68 |
| Al, P/NiWS-c@NF | 154 | 256 | — | 42 | — |

structure of the heterostructure was modulated, boosting the charge transference and improving the catalytic features of the $Ni_3S_2/WS_2$ heterostructure. Therefore, Al, P/NiWS-b@NF could be credited with promoting HER activity for the following reasons: (a) defects in Al, P/NiWS-b@NF provided active sites and a high charge transfer rate between $Ni_3S_2/WS_2$ heterojunctions, resulting in rapid NiWS-b@NF catalytic kinetics. Consequently, the HER activity was further accelerated with a small Tafel slope after a low overpotential was achieved. Due to its thin petal-like structure, $Ni_3S_2/WS_2$ exposes more active sites with a large ECSA and reduces charge transfer distance, which increases reactant accessibility. Lastly, the co-existence of $WS_2$ and $Ni_3S_2$ phases and the co-doping of Al, P ions at the heterointerface resulted in numerous lattice defects that enhanced hydrogen adsorption. This dual-doping strategy not only increases the number of active sites but also optimizes the electronic properties of the material, resulting in a more efficient HER.

Further, electrocatalyst stability is important for practical applications. The long-term catalytic stability and durability of the Al, P/NiWS-b@NF, Al/NiWS@NF, P/NiWS@NF, NiWS@NF, and Pt/C@NF (20% wt) were assessed by chronoamperometric analysis at $-180$ $mV_{RHE}$ (Fig. 5a). According to Fig. S9,† commercial 20% Pt/C showed a 59.40% drop in current density after continuous electrocatalysis for 12 h in 0.5 M $H_2SO_4$ electrolyte. Current loss can be caused by several factors during a long-term stability test. Long-term immersion in a solution and the presence of gas bubbles could lead to the creation of adsorption products that would block activity or result in peeling away of low-dimensional nanostructures. Fig. 5a depicts the 12 hour chronopotentiometric durability test at a cathodic current density of 20 mA cm$^{-2}$. The fact that there were no substantial fluctuations in starting current during the test indicates good stability.

To further examine the durability of the Al, P/NiWS-b@NF electrodes, a deterioration test in 0.5 M $H_2SO_4$ was carried out with potential sweeps from $-0.7$ to +0.2 V for 2000 cycles. As demonstrated in Fig. 5b, the LSV curves prior to and following 2000 cycles show a nearly negligible drop in current density, with a slight change of only around 10 mV at current density of 20 mA cm$^{-2}$, which reveals a good stability of the Al, P/NiWS-b@NF catalyst, agreeing with Tafel plot measurements, where no increase in the Tafel slope was exhibited after cycling (inset in Fig. 5b, left). The morphology, crystal structure, and stability of Al, P/NiWS-b@NF samples were investigated using HR-SEM and XRD after the 12 h chronoamperometry test. As shown in Fig. 5c, the hierarchical and morphological structure of Al, P/NiWS@NF is stable after long-term testing. Furthermore, the XRD pattern showed that the Al, P/NiWS-b@NF heterostructure retained its crystal structure (Fig. 5d). The reduction in $WS_2$ peak intensity might be attributed to the exfoliation of $WS_2$ nanosheets. It has been shown that Al, P/NiWS-b@NF electrodes are both a promising and cost-effective option for HER applications. A comparison of the electrocatalytic properties of Al, P/NiWS@NF with other catalysts that have been reported in the literature can be found in Table 2. Particularly, the HER activity of our catalyst was significantly higher than that of other catalysts, resulting in a lower overpotential and a higher current density. Several synergies in the elaborate morphological structure, along with electronic and interfacial interactions, are responsible for the superior activity of Al, P/NiWS@NF. Strongly coupled $WS_2$ nanosheets and $NiS/Ni_3S_4$ nanoparticles combined in a hierarchical framework provide maximum exposure to active heterogeneous interfaces as well as efficient mass and electron transfer. It has been recognized that *in situ* aluminum and phosphorus introductions are highly effective strategies for activating the inert basal plane and promoting the edge sites' activity of 2D $WS_2/MoS_2$ and other metal sulfides.[49–52] As a result of the P dopant, metal sulfides can display an increase in valence bandwidth as well as higher density of states around Fermi levels, thereby enhancing conductivity.[20,52] Additionally, Al decoration of metal sulfides, such as $MoS_2$, may lead to a reduction in bandgaps, hence improving the intrinsic conductivity of nanodomains and allowing the conjunction of positive protons and catalysts, resulting in enhanced HER performance.[53,54] Based on understanding the active origin of the Al, P/NiWS-b@NF catalyst, a rough estimation of its turnover frequency (TOF) was made, one of the most important criteria for evaluating an electrocatalyst's intrinsic performance. A further verification of the mass activities was carried out to determine the intrinsic characteristics of Al, P/NiWS-b@NF. In Note S1,† the specific calculation process for TOF and mass activities is described. By adding Al, P doping to NiWS-b@NF, mass activity increased from 112 A g$^{-1}$ at 0.3 V *vs.* RHE to 575 A g$^{-1}$ at 0.3 V *vs.* RHE (Table S3†). The acquired parameters are clearly in agreement with the CV, Tafel, and EIS results. As the benchmark HER catalyst, Pt/C displayed the TOF values of 0.772 s$^{-1}$ at overpotentials of 0.300 V, respectively, in the 0.5 M

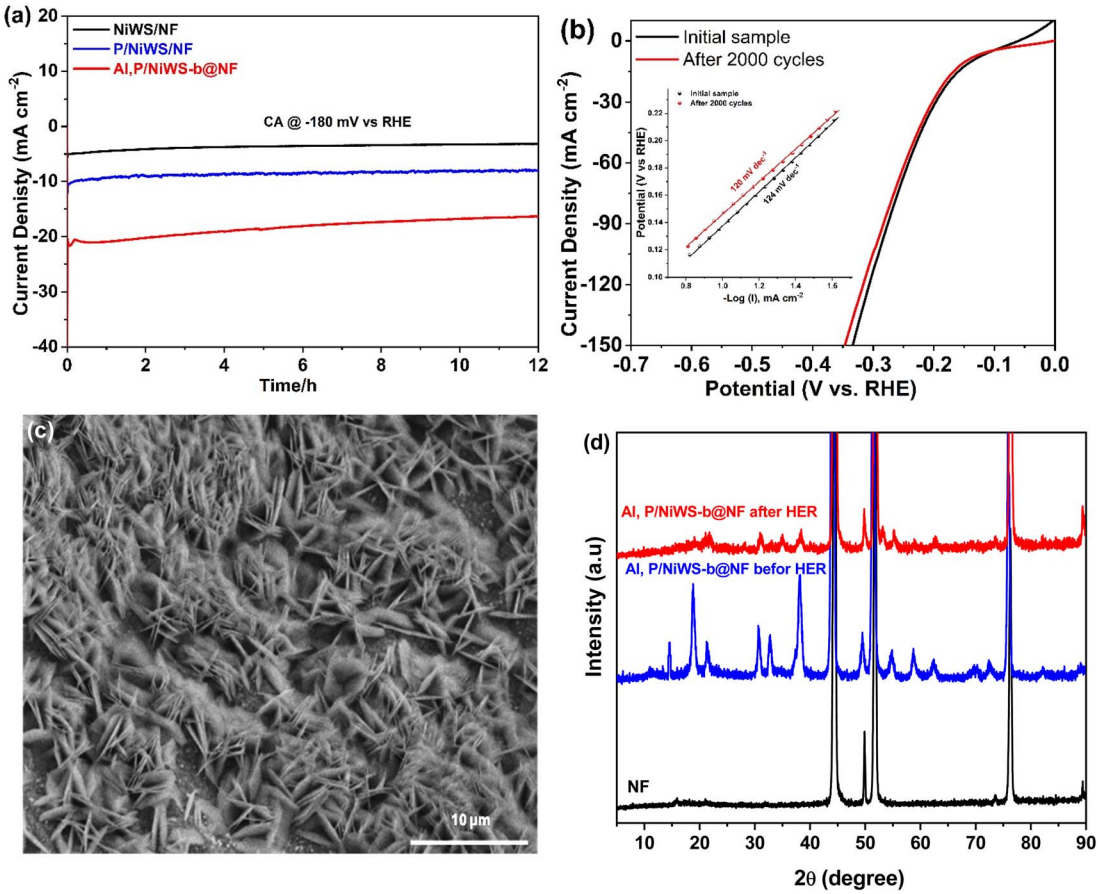


Fig. 5 (a) The chronoamperometry of NiWS@NF, P/NiWS@NF, and Al, P/NiWS-b@NF electrodes measured for 12 hours at −180 mV *vs.* RHE in 0.5 M $H_2SO_4$. (b) LSV curves of the Al, P/NiWS-b@NF before and after 2000 CV cycles with a potential range from 0.2–0.7 V *vs.* RHE. Inset: Tafel plots recorded from Al, P/NiWS-b@NF catalyst before and after 2000 potential cycles (c) HR-SEM images of Al, P/NiWS-b@NF sample after 12 h chronoamperometry test. (d) XRD patterns of Al, P/NiWS-b@NF sample before and after 12 h chronoamperometry test.

$H_2SO_4$ electrolyte. Al, P/NiWS-b@NF catalysts required overpotentials of 0.300 V to achieve TOF values of 0.8 $s^{-1}$, which is greater than that required for other investigated electrocatalysts in the same electrolyte, shown in Table S1.† It is evident that the Al, P/NiWS-b@NF electrodes perform significantly better than the investigated electrocatalysts. These results evidence that Al, P/NiWS-b@NF strongly enhanced the electrochemical performance of electrochemical HERs. Overall, Al, P/NiWS-b@NF

Table 2 Data comparison for the electrocatalytic performance of many identified catalysts, was linked to the present study for HER

| Electrocatalyst | Electrode reaction | Electrolyte | Overpotential (mV) at −10 mA $cm^{-2}$ | Tafel slope (mV $dec^{-1}$) | Substrate/preparation method | Ref. |
|---|---|---|---|---|---|---|
| $WS_2NS_2$ | HER | 0.5 M $H_2SO_4$ | −150 | 138 | Glassy carbon/mechanical activation method | 55 |
| $Fe_xS_y/WS_2$ Ns | HER | 0.5 M $H_2SO_4$ | −118 | 87 | Glassy carbon/hydrothermal method | 56 |
| $MoS_2/WS_2$ | HER | 0.5 M $H_2SO_4$ | −280 | 53 | Glassy carbon/hydrothermal method | 57 |
| NiS–$NiS_2$–$Ni_3S_4$ | HER | 1 M KOH | −68 | 79 | Nickel foam/hydrothermal sulfidation method | 58 |
| Fe-doped $WS_2$ | HER | 0.5 M $H_2SO_4$ | −166 | 82.2 | Carbon cloth/solvothermal method | 59 |
| $Ni_3S_2$@$Ni_2P/MoS_2$/NF | HER | 1 M KOH | −160 | 103.6 | Nickel foam/hydrothermal phosphating method | 60 |
| Ni/$Ni_3S_2$/SC NSAs | HER | 0.5 M $H_2SO_4$ | −90 | 81 | Carbon cloth/hydrothermal method | 61 |
| $Ni_3S_2$@NiSe/NF | HER | 0.5 M $H_2SO_4$ | −103 | 74.2 | Nickel foam/thermal diffusion method | 62 |
| Al, P/NiWS-b@NF | HER | 0.5 M $H_2SO_4$ | −136 @ 10 mA $cm^{-2}$ −227 @ 50 mA $cm^{-2}$ | 124 | Nickel foam/hydrothermal method | This work |

electrode materials have a high potential for storage of energy and conversion devices due to their increased HER properties.

## 4. Conclusion

In conclusion, the hydrothermal approach was employed for constructing an Al, P/NiWS-*x*@NF heterostructure on NF. Because of the advantageous heterostructural properties, particularly the nanoparticles/nanosheets structured as well as optimizing Al, and P co-doping concentrations, Al, P/NiWS-b@NF showed excellent electrocatalytic performance towards HER with a small Tafel slope (~128 mV $dec^{-1}$), and an overpotential of only 136 mV to obtain a current density of 10 mA $cm^{-2}$ in acidic media. Based on the experimental results, the combination of Al and P co-doping with $NiS/Ni_3S_2/WS_2$ heterostructure led to superb acidic HER performance and exceptional durability. A hierarchical structure facilitates fast charge/mass transport and maximizes active heterointerface accessibility. The present work demonstrates a method for boosting hydrogen desorption by synergistically combining multiple components, thus accelerating the $H_2$ evolution.

## Data availability

The data supporting this article have been included as part of the ESI.†

## Author contributions

Mghaib Al Shahrani: data curation, formal analysis, investigation. Mabrook S. Amer: conceptualization, writing – review & editing, data curation, supervision. Ahmad A. Alsaleh: data curation, writing – review & editing, Prabhakarn Arunachalam: data curation, writing – review & editing, Abdullah M. Al-Mayouf: supervision, funding acquisition, project administration.

## Conflicts of interest

The authors declare that they have no known competing financial interests or personal relationships that could have appeared to influence the work reported in this paper.

## Acknowledgements

This research was supported by the Researchers Supporting Project number (RSPD2024R540) at King Saud University, Riyadh, Saudi Arabia.

## References

1 H. B. Gray, *Nat. Chem.*, 2009, **1**, 7.
2 V. R. Stamenkovic, D. Strmcnik, P. P. Lopes and N. M. Markovic, *Nat. Mater.*, 2017, **16**, 57–69.
3 M. S. Dresselhaus and I. Thomas, *Nature*, 2001, **414**, 332–337.
4 D. Niblett, M. Delpisheh, S. Ramakrishnan and M. Mamlouk, *J. Power Sources*, 2024, **592**, 233904.
5 B. You and Y. Sun, *Acc. Chem. Res.*, 2018, **51**, 1571–1580.
6 P. Arunachalam, M. S. Amer, A. M. Al-Mayouf and A. A. Alsaleh, *ChemCatChem*, 2024, **16**(14), e202400312.
7 P. Arunachalam, M. N. Shaddad, M. S. Amer, A. M. Alsalman and J. Madhavan, *Environ. Sci.: Nano*, 2024, **11**(6), 2668–2682.
8 M. S. Amer, P. Arunachalam, A. M. Al-Mayouf, A. A. AlSaleh and Z. A. Almutairi, *Environ. Res.*, 2023, **236**, 116818.
9 J. Li, J. Zhang, J. Zhang, K. M. Pan, H. Xu, H. Chen, G. Liu, N. Wu, C. Yuan and X. Liu, *J. Mater. Chem. A*, 2023, **11**, 19812–19844.
10 M. S. Faber and S. Jin, *Energy Environ. Sci.*, 2014, **7**, 3519–3542.
11 Y. Jiao, Y. Zheng, M. Jaroniec and S. Z. Qiao, *Chem. Soc. Rev.*, 2015, **44**, 2060–2086.
12 Y. Jiao, Y. Zheng, M. Jaroniec and S. Z. Qiao, *Chem. Soc. Rev.*, 2015, **44**, 2060–2086.
13 T. Ling, T. Zhang, B. Ge, L. Han, L. Zheng, F. Lin, Z. Xu, W. B. Hu, X. W. Du and K. Davey, *Adv. Mater.*, 2019, **31**, 1807771.
14 J. Xie and Y. Xie, *Chem.–Eur. J.*, 2016, **22**, 3588–3598.
15 X. Y. Yu and X. W. Lou, *Adv. Energy Mater.*, 2018, **8**, 1701592.
16 M. S. Amer, P. Arunachalam, A. M. Al-Mayouf, A. A. Alsaleh, M. Alshalwi and Z. A. Almutairi, *ACS Appl. Energy Mater.*, 2023, **6**, 11718–11731.
17 L. Zhang, J. Xiao, H. Wang and M. Shao, *ACS Catal.*, 2017, **7**, 7855–7865.
18 Y. Guo, T. Park, J. W. Yi, J. Henzie, J. Kim, Z. Wang, B. Jiang, Y. Bando, Y. Sugahara and J. Tang, *Adv. Mater.*, 2019, **31**, 1807134.
19 C. Huang, X. Miao, C. Pi, B. Gao, X. Zhang, P. Qin, K. Huo, X. Peng and P. K. Chu, *Nano Energy*, 2019, **60**, 520–526.
20 D. Wu, S. Xu, M. Li, C. Zhang, Y. Zhu, Y. Xu, W. Zhang, R. Huang, R. Qi and L. Wang, *J. Mater. Chem. A*, 2015, **3**, 16695–16707.
21 L.-L. Feng, G. Yu, Y. Wu, G.-D. Li, H. Li, Y. Sun, T. Asefa, W. Chen and X. Zou, *J. Am. Chem. Soc.*, 2015, **137**, 14023–14026.
22 Y. Liu, H. Zhang, W. Song, Y. Zhang, Z. Hou, G. Zhou, Z. Zhang and J. Liu, *Chem. Eng. J.*, 2023, **451**, 138905.
23 H. Wang, X. Xu, B. Ni, H. Li, W. Bian and X. Wang, *Nanoscale*, 2017, **9**, 15895–15900.
24 S. Chandrasekaran, L. Yao, L. Deng, C. Bowen, Y. Zhang, S. Chen, Z. Lin, F. Peng and P. Zhang, *Chem. Soc. Rev.*, 2019, **48**, 4178–4280.
25 Q. Lu, H. Wu, X. Zheng, Y. Cao, J. Li, Y. Wang, H. Wang, C. Zhi, Y. Deng and X. Han, *Adv. Energy Mater.*, 2022, **12**, 2202215.
26 J. Zhang, T. Wang, D. Pohl, B. Rellinghaus, R. Dong, S. Liu, X. Zhuang and X. Feng, *Angew. Chem.*, 2016, **128**, 6814–6819.
27 P. Zhai, Y. Zhang, Y. Wu, J. Gao, B. Zhang, S. Cao, Y. Zhang, Z. Li, L. Sun and J. Hou, *Nat. Commun.*, 2020, **11**, 5462.
28 Q. Xu, J. Zhang, H. Zhang, L. Zhang, L. Chen, Y. Hu, H. Jiang and C. Li, *Energy Environ. Sci.*, 2021, **14**, 5228–5259.
29 S. X. Leong, C. C. Mayorga-Martinez, X. Chia, J. Luxa, Z. Sofer and M. Pumera, *ACS Appl. Mater. Interfaces*, 2017, **9**, 26350–26356.

30 X. Guo, J. Ji, Q. Jiang, L. Zhang, Z. Ao, X. Fan, S. Wang, Y. Li, F. Zhang, G. Zhang and W. Peng, *ACS Appl. Mater. Interfaces*, 2017, **9**, 30591–30598.
31 L. Sun, M. Gao, Z. Jing, Z. Cheng, D. Zheng, H. Xu, Q. Zhou and J. Lin, *Chem. Eng. J.*, 2022, **429**, 132187.
32 Y. Gu, A. Wu, Y. Jiao, H. Zheng, X. Wang, Y. Xie, L. Wang, C. Tian and H. Fu, *Angew. Chem., Int. Ed.*, 2021, **60**(12), 6673–6681.
33 B. Rehman, K. M. M. D. K. Kimbulapitiya, M. Date, C. T. Chen, R. H. Cyu, Y. R. Peng and Y. L. Chueh, *ACS Appl. Mater. Interfaces*, 2024, **16**, 32490–32502.
34 H. Chen, M. Hu, X. Wang, X. Xu, P. Jing, B. Liu and J. Zhang, *Small Struct.*, 2023, **4**, 2300026.
35 S. Ponnada, M. S. Kiai, D. B. Gorle, R. S. Bose, V. Rajagopal, B. Saini and R. K. Sharma, *Catal. Sci. Technol.*, 2022, **12**(14), 4413–4441.
36 H. Wang, M. Ma, J. Li, Z. Zhang, W. Zhou and H. Liu, *J. Mater. Chem. A*, 2021, **9**, 25539–25546.
37 H. Liu, Z. Liu, F. Wang and L. Feng, *Chem. Eng. J.*, 2020, **397**, 125507.
38 C. Dai, B. Li, J. Li, B. Zhao, R. Wu, H. Ma and X. Duan, *Nano Res.*, 2020, **13**, 2506–2511.
39 K. Tang, X. Wang, Q. Li and C. Yan, *Adv. Mater.*, 2018, **30**, 1704779.
40 X. Lu, R. Liu, Q. Wang and C. Xu, *ACS Appl. Mater. Interfaces*, 2019, **11**, 40014–40021.
41 Y. Yang, H. Yao, Z. Yu, S. M. Islam, H. He, M. Yuan, Y. Yue, K. Xu, W. Hao and G. Sun, *J. Am. Chem. Soc.*, 2019, **141**, 10417–10430.
42 P. Zhou, P. K. Wong, P. Niu, M. Chen, C. T. Kwok, Y. Tang, R. Li, S. Wang and H. Pan, *Sci. China Mater.*, 2023, **66**, 1033–1041.
43 M. Wang, W. Zhang, F. Zhang, Z. Zhang, B. Tang, J. Li and X. Wang, *ACS Catal.*, 2019, **9**, 1489–1502.
44 B. He, C.-Q. Peng, F. Ye, H.-W. Gao, Y. Wang, Y.-W. Tang, Q.-L. Hao, H.-K. Liu and Z. Su, *CrystEngComm*, 2021, **23**, 3861–3869.
45 Z. Fang, L. Peng, Y. Qian, X. Zhang, Y. Xie, J. J. Cha and G. Yu, *J. Am. Chem. Soc.*, 2018, **140**, 5241–5247.
46 Z. Liu, K. Wang, Y. Li, S. Yuan, G. Huang, X. Li and N. Li, *Appl. Catal., B*, 2022, **300**, 120696.
47 P. Yu, F. Wang, T. A. Shifa, X. Zhan, X. Lou, F. Xia and J. He, *Nano Energy*, 2019, **58**, 244–276.
48 C. Wang, T. Wang, J. Liu, Y. Zhou, D. Yu, F. Han, Q. Li, J. Chen and Y. Huang, *Energy Environ. Sci.*, 2018, **11**, 2467–2475.
49 P. Liu, J. Zhu, J. Zhang, P. Xi, K. Tao, D. Gao and D. Xue, *ACS Energy Lett.*, 2017, **2**, 745–752.
50 D. Ren, Z. Liang, Y. H. Ng, P. Zhang, Q. Xiang and X. Li, *Chem. Eng. J.*, 2020, **390**, 124496.
51 L. Sun, M. Gao, Z. Jing, Z. Cheng, D. Zheng, H. Xu, Q. Zhou and J. Lin, *Chem. Eng. J.*, 2022, **429**, 132187.
52 D. R. Paudel, U. N. Pan, T. I. Singh, C. C. Gudal, N. H. Kim and J. H. Lee, *Appl. Catal., B*, 2021, **286**, 119897.
53 J. Jian, Y. Li, H. Bi, X. Wang, X. Wu and W. Qin, *ACS Sustain. Chem. Eng.*, 2020, **8**, 4547–4554.
54 J. Jian, H. Kang, X. Qiao, K. Cui, Y. Liu, Y. Li, W. Qin and X. Wu, *ACS Sustain. Chem. Eng.*, 2022, **10**, 10203–10210.
55 Z. Wu, B. Fang, A. Bonakdarpour, A. Sun, D. P. Wilkinson and D. Wang, *Appl. Catal., B*, 2012, **125**, 59–66.
56 H. Chen, Y. Li, H. Huang, Q. Kang and T. Ma, *Energy Fuels*, 2022, **36**, 4888–4894.
57 D.-z. WANG, Y. Liu-yi-yi, R.-q. LIU, G. Ting, F. Hao and Z.-z. WU, *Trans. Nonferrous Met. Soc. China*, 2023, **33**, 1540–1549.
58 H. Wang, W. Zhang, X. Zhang, S. Hu, Z. Zhang, W. Zhou and H. Liu, *Nano Res.*, 2021, **14**, 4857–4864.
59 X. Pu, J. Qian, J. Li, D. Gao and R. Zhang, *FlatChem*, 2021, **29**, 100278.
60 X. Yu, S. Xu, Z. Wang, S. Wang, J. Zhang, Q. Liu, Y. Luo, Y. Du, X. Sun and Q. Wu, *Dalton Trans.*, 2021, **50**, 15094–15102.
61 Y. Li, D. M. Patel, C. S. Tsang, R. Zhang, M. Liu, G. S. Hwang and L. Y. S. Lee, *Adv. Mater. Interfaces*, 2021, **8**, 2001665.
62 N. Shaikh, I. Mukhopadhyay and A. Ray, *J. Mater. Chem. A*, 2022, **10**, 12733–12746.